Author/s:
Liang, RZ;Babics, M;Seitkhan, A;Wang, K;Geraghty, PB;Lopatin, S;Cruciani, F;Firdaus, Y;Caporuscio, M;Jones, DJ;Beaujuge, PM

Title:
Additive-Morphology Interplay and Loss Channels in “All-Small-Molecule” Bulk-heterojunction (BHJ) Solar Cells with the Nonfullerene Acceptor IDTTBM

Date:
2018-02-14

Citation:
Liang, R. Z., Babics, M., Seitkhan, A., Wang, K., Geraghty, P. B., Lopatin, S., Cruciani, F., Firdaus, Y., Caporuscio, M., Jones, D. J. & Beaujuge, P. M. (2018). Additive-Morphology Interplay and Loss Channels in “All-Small-Molecule” Bulk-heterojunction (BHJ) Solar Cells with the Nonfullerene Acceptor IDTTBM. Advanced Functional Materials, 28 (7), https://doi.org/10.1002/adfm.201705464.

Persistent Link:
https://hdl.handle.net/11343/294035

DOI: 10.1002/ ((please add manuscript number))

Article type: Full Paper

Additive-Morphology Interplay & Loss Channels in “All-Small-Molecule” BHJ Solar Cells with the Nonfullerene Acceptor IDTTBM

Ru-Ze Liang, Maxime Babics, Akmaral Seitkhan, Kai Wang, Paul Bythal Geraghty, Sergei Lopatin, Federico Cruciani, Yuliar Firdaus, Marco Caporuscio, David J. Jones, and

*Pierre M. Beaujuge**

R.-Z. Liang, M. Babics, A. Seitkhan, Dr. K. Wang, F. Cruciani, Dr. Y. Firdaus, M. Caporuscio, and Prof. P. M. Beaujuge

Physical Sciences and Engineering Division
KAUST Solar Center (KSC)
Dr. S. Lopatin

Imaging and Characterization Laboratory

King Abdullah University of Science and Technology (KAUST)
Thuwal 23955-6900, Saudi Arabia
E-mail: pierre.beaujuge@kaust.edu.sa

P. B. Geraghty, and Prof. D. J. Jones
School of Chemistry, Bio21 Institute,

The University of Melbourne
Parkville, Victoria 3010, Australia

Keywords: small molecules, nonfullerenes, bulk heterojunctions, solar cells, organic photovoltaics.

Abstract

Achieving efficient bulk-heterojunction (BHJ) solar cells from blends of solution-processable small-molecule (SM) donors and acceptors has proven particularly challenging due to the complexity in obtaining a favorable donor-acceptor morphology. In this report, we examine the BHJ device performance pattern of a set of analogous, well-defined SM donors – **DR3TBDTT** (**DR3**), **SMPV1**, and **BTR** – used in conjunction with the SM acceptor **IDTTBM**. Our examinations show that the nonfullerene "All-SM" BHJ solar cells made with **DR3** and **IDTTBM** can achieve power conversion efficiencies (PCEs) of up to *ca.* 4.5% (avg. 4.0%) when the solution-processing additive 1,8-diiodooctane (DIO, 0.8% v/v) is used in the blend solutions. The figures of merit of optimized **DR3:IDTTBM** solar cells contrast with those of "*as-cast*" BHJ devices from which only modest PCEs <1% can be achieved. Combining electron energy loss spectrum (EELS) analyses in scanning transmission electron microscopy (STEM) mode, carrier transport measurements via "metal-insulator-semiconductor carrier extraction" (MIS-CELIV) methods, and systematic recombination

examinations by light-dependence and transient photocurrent (TPC) analyses, we show that DIO plays a determining role – establishing a favorable lengthscale for the phase-separated SM donor-acceptor network and, in turn, improving the balance in hole/electron mobilities and the carrier collection efficiencies overall.

1. Introduction

While Solution-processable, π-extended small molecules (SM) are promising alternatives to their evaporated SM counterparts and to polymers[1-2] in bulk-heterojunction (BHJ) solar cells. The demonstrations that (i) SM donors can rival polymers in fullerene-based BHJ device configurations,[3-7] while (ii) SM acceptors can effectively replace and outperform fullerenes (*e.g.* phenyl-C_{61}-butyric acid methyl ester, $PC_{61}BM$; or its C_{71} analogue, $PC_{71}BM$) in BHJ solar cells,[8-10] are however fairly recent.[9, 11-12] For either material combinations, achieving a favorable donor-acceptor morphology in BHJ thin films is the efficiency-determining step.[7, 13-15] Often times, the use of solution-processing additives[6, 14, 16] and post-processing treatments, including thermal[17] and solvent-vapor annealing processes,[18-20] can help reach more adequate BHJ networks – usually by mediating the lengthscale of phase-separation between donor and acceptor.[13, 21-22]

The perspective of achieving efficient BHJ solar cells by combining solution-processable SM donors and acceptors (nonfullerenes) is even more recent,[9, 11-12, 23-24, 25-26] as earlier attempts have commonly met with limited success.[9, 11-12, 27] In general, the high degree of crystallinity (or lack thereof, in some instances) inherent to the SM systems being concurrently cast as a single precursor solution governs the development of the BHJ thin-film morphology, leading to oversized (crystalline) domains with limited connectivity[21] and insufficient donor-acceptor mixing,[21-22] or on the contrary, to excess (amorphous) donor-acceptor mixing and hindered carrier extraction.[22, 28] In this context, the use of external solution-processing additives and/or post-processing treatments may help leverage more favorable BHJ morphologies and, in turn, improved solar cell power conversion efficiencies (PCEs). Compared to polymers, π-extended SM systems – donors and nonfullerene acceptors – have well-defined structures, while being synthetically scalable following cost-effective methods and processes.[22] Thus, nonfullerene "All-SM" BHJ solar cells that can rival polymer and/or fullerene-based device strategies are expected to become increasingly relevant.

In this contribution, we examine the BHJ solar cell performance pattern of a set of analogous SM donors – **DR3TBDTT** (**DR3**), **SMPV1**, and **BTR** (Chart 1) – used in conjunction with the SM acceptor **IDTTBM** (Chart 1; cf. synthetic details provided in the Supporting Information, SI). The SM donors have the same π-conjugated main chain composition, but differ by the pattern of solubilizing side-chains appended to the heterocyclic motifs. In polymer-fullerene BHJ solar cells, the polymer side-chain pattern plays a determining role, impacting backbone self-assembly, aggregation and mediating intermolecular interactions between the polymer donor and the fullerene acceptor.[29-

31] Thus, turning to the examination of SM donors with nonfullerene SM acceptors, the systematic study of how side-chain substituents may influence the propensity of the SM blends to form favorable donor-acceptor morphologies and yield efficient "All-SM" BHJ solar cells may provide some general guiding principles for the selection of the SM donor with respect to the nonfullerene acceptors that are currently proving particularly promising (such as ITIC,[32] **IDTTBM**[10] and others[33]**)**. It should also be noted that all of the three SM donors examined in this study: **DR3**,[34] **SMPV1**,[35] and **BTR**,[5, 36] can yield PCEs >6% in SM-fullerene BHJ solar cells, and are therefore sensible candidates in this systematic study with the nonfullerene acceptor **IDTTBM (**PCEs >8% with the model polymer donor PCE10; cf. details in the SI, Table S7**).** Of all donor-acceptor combinations, we find that All-SM solar cells made with **DR3** and **IDTTBM** can achieve PCEs as high as *ca.* 4.5% (avg. 4.0%) when the solution-processing additive 1,8-diiodooctane (DIO, 0.8% v/v) is used in the blend solutions. In comparison, "*as-cast*" BHJ devices yield only modest PCEs <1%, pointing to the determining role of the processing additive DIO. Combining electron energy loss spectrum

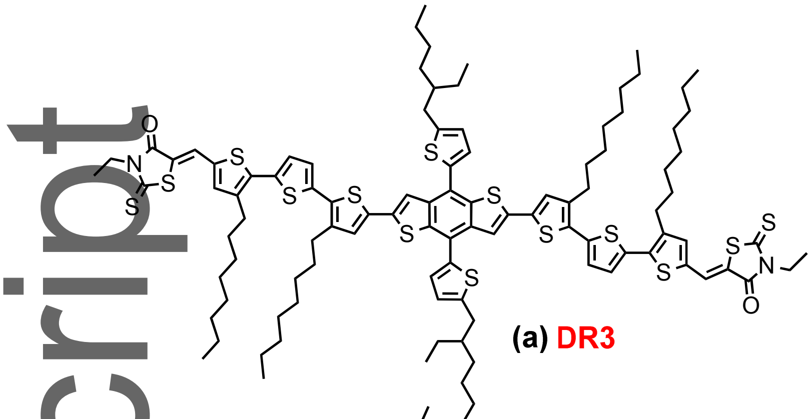

(a) DR3

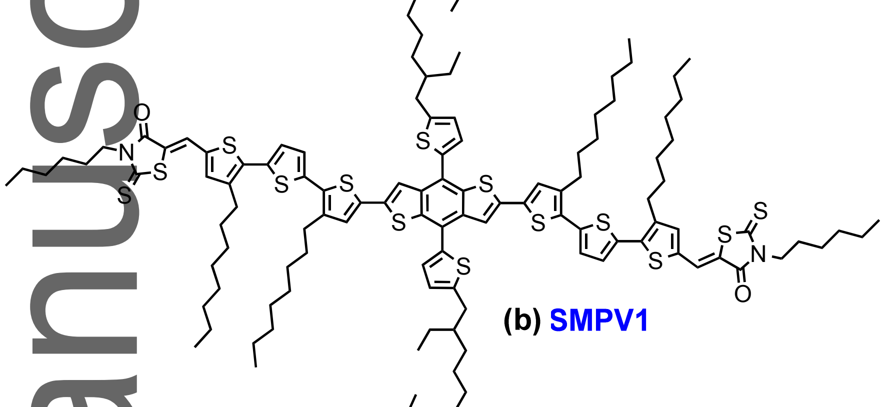

(b) SMPV1

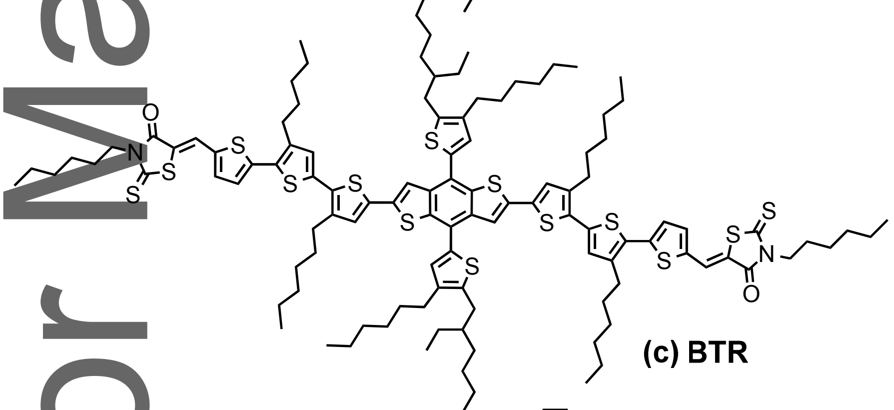

(c) BTR

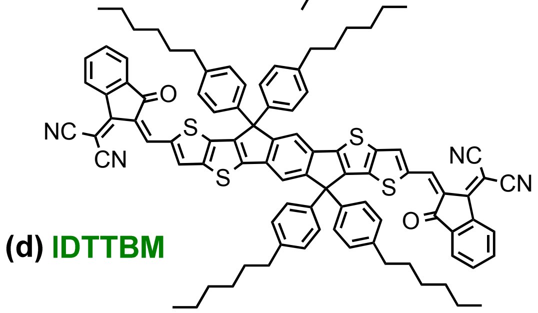

(d) IDTTBM

Chart 1. Molecular Structures of the Set of Analogous SM Donors (a) **DR3**, (b) **SMPV1**, and (c) **BTR**, and that of the Nonfullerene Acceptor (d) **IDTTBM**.

(EELS) analyses in scanning transmission electron microscopy (STEM) mode, carrier transport measurements via “metal-insulator-semiconductor carrier extraction” (MIS-CELIV) methods, and systematic recombination examinations by light-dependence and transient photocurrent (TPC) analyses, we detail the influence of the processing additive DIO on the development of the phase-separated donor-acceptor network, comparing “*as-cast*” and “optimized” All-SM active layers. We find that both carrier transport and bimolecular recombination patterns improve notably in optimized BHJ active layers compared to “*as-cast*” films, and show that **DR3**- and **SMPV1**-based All-SM devices benefit from a greater balance in hole/electron mobilities and higher carrier collection efficiencies compared to their **BTR** counterparts. Although challenges exist in the determination and direct visualisation of favorable BHJ morphologies, [9, 23-26, 37-38] our characterization approach using spatially-resolved electron energy loss spectrum (EELS) techniques allows for effectively probing the phase distribution of the nonfullerene “All-SM” solar cells studied in this work, with a look on how adding DIO as processing additive to the blend affects moprhologies and device efficiency. In turn, our approach to the morphological analysis of nonfullerene “All-SM” solar cells should be applicable to other material systems and BHJ solar cell optimization studies.

2. Results and Disscusion

2.1. Material Properties

The normalized thin-film UV-vis absorption spectra of the SM donors **DR3, SMPV1, BTR** and the nonfullerene acceptor **IDTTBM** are overlaid in Figure 1a; temperature-dependent solution UV-vis spectra are provided in Figures S2. Based on those analyses, all three SM donors have comparable absorption patterns shifting to longer wavelengths (by *ca.* 100 nm) on going from solutions to films (Figures S1). The spectral features of the main absorption band and the significant bathochromic shift observable in the neat films suggest that the SM donors are prone to aggregate; the visible reduction in peak intensity at higher temperatures in the UV-vis spectra is another indication that some extent of aggregation occurs, even at the low concentration used for this experiment (1x10^{-5} M). The extended thin-film absorption of the SM donors across the

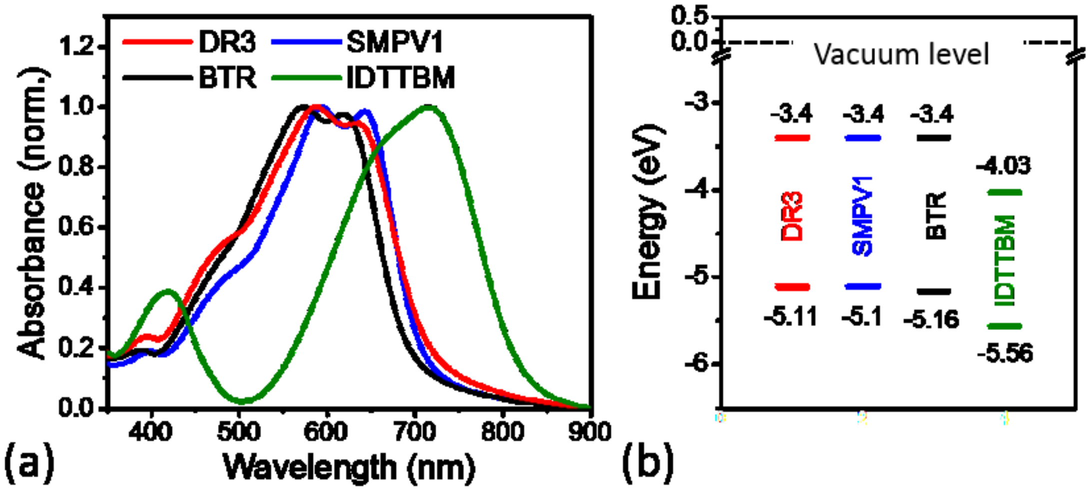

Figure 1. (a) Normalized thin-film UV-vis absorbance spectra, and (b) PESA-estimated ionization potentials (IP) and electron affinity (EA) for **DR3**, **SMPV1**, **BTR**, and **IDTTBM**. EA values inferred by subtracting IP and E_{opt} values (optical bandgaps estimated from the onset of the UV-vis absorption spectra (films)).

range 500-700 nm make them especially relevant as complementary absorbers with the nonfullerene SM acceptor **IDTTBM** which has its main band of absorption in the range 600-800 nm). Figures 1b provides the expected energy band offsets for the SM donors with **IDTTBM**; the optical bandgaps (E_{opt}) are inferred from the onset of the thin-film UV-vis absorption spectra: ca. 1.71 eV for **DR3**, ca. 1.70 eV for **SMPV1**, ca. 1.76 eV for **BTR**, and ca. 1.53 eV for **IDTTBM**; the

Table 1. Summary of Optical and Electronic Parameters for the SM donors **DR3**, **SMPV1**, and **BTR**, and for the Nonfullerene Acceptor **IDTTBM**.

SM	λ_{abs}/sol (nm) (log ε)	λ_{abs}/film (nm)	E_{opt} [a] (eV)	IP [b] (eV)	EA [c] (eV)
DR3	508 (4.89)	588	1.71	5.11	3.4
SMPV1	508 (4.95)	594	1.7	5.1	3.4
BTR	519 (4.92)	572	1.76	5.16	3.4
IDTTBM	663 (4.92)	716	1.53	5.56	4.03

[a] Optical bandgaps estimated from the onset of the UV-vis absorption spectra (films); [b] Estimated by photoelectron spectroscopy (PESA); [c] Inferred from PESA-estimated IPs and E_{opt} values.

ionization potentials (IPs) for the SMs were determined via photoelectron spectroscopy in air (PESA, cf. experimental details in the SI): 5.11 eV for **DR3**, 5.10 eV for **SMPV1**, 5.16 eV for **BTR**, and 5.56 eV for **IDTTBM**. These figures are summarized in Table 1, along with extrapolated electron affinity (EA) values inferred by subtracting IP and E_{opt} values.

2.2. Device Testing and Characterizations

Thin-film BHJ solar cells were fabricated with the inverted structure ITO/a-ZnO/SM:**IDTTBM**/MoO_3/Ag (device area: 0.1 cm^2), and tested under simulated AM1.5G sun illumination (100 mW/cm^2); detailed experimental protocols are provided in the SI. Table 2 summarizes the figures of merit of optimized BHJ devices made from blends of the SM donors **DR3, SMPV1, BTR** and the nonfullerene acceptor **IDTTBM**, with and without addition of the

Table 2. PV Performance of the SM Donors **DR3**, **SMPV1**, and **BTR** in Inverted BHJ Devices with the Nonfullerene SM Acceptor **IDTTBM**.^{a}

SM	DIO %(v/v)	J_{SC} [mA/cm^{2}]	V_{OC} [V]	FF [%]	Avg. PCE^{d} [%]	Max. PCE [%]
DR3^{b}	0	3.4	0.75	28	0.6	0.8
	0.8^{e}	9.3	0.9	48	4	4.4
SMPV1^{b}	0	3.2	0.78	27	0.6	0.7
	0.8^{e}	9.4	0.91	48	4.1	4.4
BTR	0^{c}	1.8	0.76	32	0.4	0.4
	0.5^{c,e}	5.9	0.88	44	2.3	2.4
	0.8^{b}	4.5	0.93	40	1.7	1.7

[a] Additional device statistics are provided in the SI (Tables S1 and S2). [b] Devices with optimized SM:**IDTTBM** ratio of 7:3 (wt/wt) solution-cast from chloroform (CF). [c] Devices with optimized SM:**IDTTBM** ratio of 6:4 (wt/wt) solution-cast from CF. [d] Average values across >20 devices (device area: 0.1 cm^{2}). [e] Optimized device conditions.

processing additive 1,8-diiodooctane (DIO) in the blend solutions; further device statistics are provided in the SI (Tables S1–S6). Solution-processing additives, including DIO and 1-chloronaphthalene (CN), have proven useful in the systematic optimizations of blend morphologies in BHJ solar cells made from SM donors and fullerene acceptors and, in turn, device PCEs.[14, 16] However, it is equally critical to note that morphological changes promoted by processing additives can also result in reduced device performance figures, and that the outcome of these tentative optimization steps remain SM system-dependent. As shown in Table 2, "*as-cast*" devices made from **DR3** and **SMPV1** yield concurrently low short-circuit current (J_{SC}), fill factor (FF) and open-circuit voltage (V_{OC}) values of 3-3.5 mA/cm^2, <30% and 0.75-0.8 V, respectively. However, upon adding 0.8% DIO (v/v) in the blend solution (cf. DIO optimization study in the SI, Table S2), the device J_{SC} and FF increase dramatically from 3-3.5 mA/cm^2 to 9-9.5 mA/cm^2 (more than a twofold increase), and from <30% to >45%, suggesting that significant, favorable morphological effects are occurring in the BHJ active layer. Interestingly, a notable increase in V_{OC} to *ca.* 0.9 V is concurrently observed – which is likely the result of morphological changes at the contact interfaces – yielding significantly improved PCEs of up to 4.4% (avg. 4%). The V_{OC} of *ca.* 0.9 V is in agreement with the difference between PESA-estimated IP of **DR3** and **SMPV1** (*ca.* 5.1 eV), and EA value of **IDTTBM** (*ca.* 4.0 eV) inferred from PESA-estimated IP and E_{opt} values. Overall, these experimental results also indicate that the end-group substitution with longer alkyls on going from **DR3** to **SMPV1** does not noticeably impact SM and BHJ device performance. In contrast, Table 2 shows that both "*as-cast*" and optimized BHJ solar cells made from **BTR** exhibit markedly lower J_{SC} values of 1.8 mA/cm^2 and 5.9 mA/cm^2, respectively. As a result, the PCEs of **BTR**-based devices are limited to 0.4% in "*as-cast*" devices and to 2.4% for optimized BHJ solar cells (cf. detailed conditions in Table 2). For all three SM donor systems, it is worth noting that, excessive volumes of DIO used in the solution blends (ranging from 1.25% to 10%) lead to inadequate film morphologies (discussed in later sections), causing device PCEs to drop to *ca.* 0% (cf. further device data in the SI, Table S2).

The higher J_{SC} values achieved with **DR3-** and **SMPV1**-based BHJ devices compared to those obtained with **BTR** (Fig. 2a) are consistent with the external quantum efficiency (EQE) spectra provided in Figure 2b. Thus, **DR3**/**SMPV1**-based devices show EQE values higher than

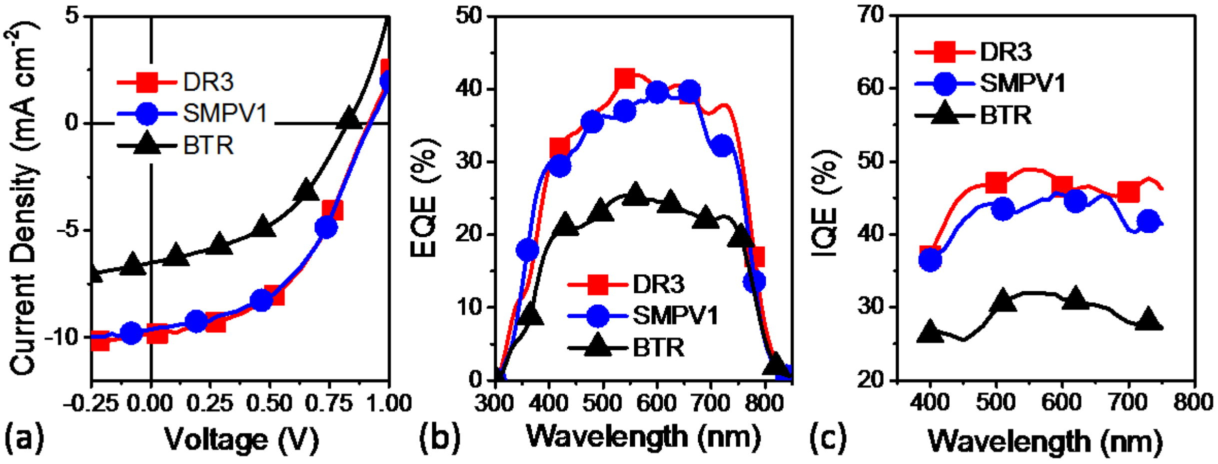

Figure 2. (a) Characteristic *J-V* curves of optimized "All-SM" BHJ solar cells fabricated from the SM donors **DR3**, **SMPV1**, and **BTR**, and the nonfullerene SM acceptor **IDTTBM** (processing conditions detailed in Table 2); AM1.5G solar illumination (100 mW/cm^2). (b) EQE and (c) IQE spectra of the optimized devices. Integrated EQEs are in agreement (± 0.7 mA/cm^2) with the J_{sc} values reported in Table 2.

those obtained with **BTR** by >10% across the range 400-750 nm (peaking at *ca.* 46% for **DR3** and *ca.* 43% for **SMPV1**; reflecting an EQE increase of more than *ca.* 50% relative to the **BTR**-based range, in agreement with the modest J_{SC} values of 5.9 mA/cm^2 measured from the *J-V* plots (Fig. 2a). Integrated EQEs are in agreement (± 0.7 mA/cm^2) with the J_{SC} values discussed above and reported in Table 2. The dependence on the effective optical absorption of the active layer is removed in comparing the internal quantum efficiency (IQE) spectra of the optimized All-SM devices), while the EQE response of **BTR**-based devices remain under 25% across the same devices shown in Figure S5; see experimental details in the SI (Section 5). Considering the film thickness measurements performed on optimized BHJ active layers (thicknesses: 110-120 nm for **DR3**, 105-115 nm for **BTR**; cf. details in the SI, Figure S7-S8), our J_{SC} predictions via transfer matrix modeling (cf. details in the SI, Fig. S6) are consistent with the trend in experimental J_{SC} vs. active layer thickness. Overall, the IQE spectra parallel the EQE, with IQE values >40% across the range 400-750 nm for **DR3**/**SMPV1**-based BHJ devices, <30% across the same range for **BTR**-based solar cells. These finding suggest that all three SM donor and **IDTTBM**-based All-SM solar cells are hindered by substantial recombination and/or exciton quenching events, limiting the photocurrents; although, these effects may not be as pronounced in **DR3/SMPV1**-based devices.

The BHJ morphologies of "*as-cast*" and "optimized" (DIO, 0.8% (v/v); conditions identical to those described in Table 2) devices made with the SM donors **DR3, SMPV1, BTR** and the nonfullerene acceptor **IDTTBM** were examined by bright-field electron transmission microscopy (TEM; cf. details in SI, Fig. S11). Figures S11 provide insights into the thin-film morphologies on various magnification scales; here, both "*as-cast*" and "optimized" active layers appear rather non-uniform at first, although we note that distinguishing between donor- and acceptor-rich domains requires a different level of analysis, and that contrast differences in the bright-field mode can also result from film thickness and/or surface roughness variations. Figures S9 and S10 examine the film surface variations by atomic force microscopy (AFM), indicating that "optimized" active layers contain rugged planes characterized by root-mean-square (RMS) roughness values >3 nm, while "*as-cast*" films have RMS values <1 nm. High-resolution TEM imaging coupled with electron energy loss spectroscopy (EELS) analyses shown

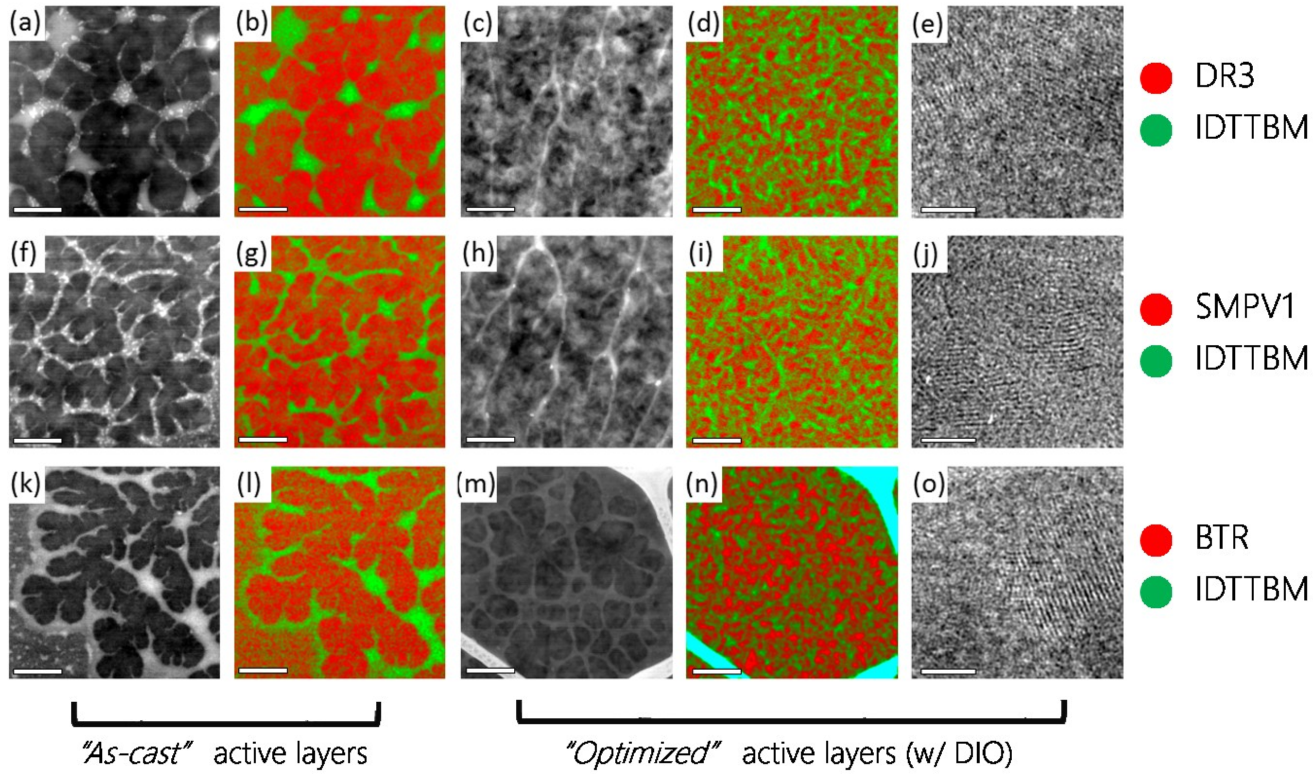

Figure 3. Morphology analyses of "All-SM" active layers made from (a-e) **DR3**, (f-j) **SMPV1** and (k-o) **BTR**, in blends with the nonfullerene SM acceptor **IDTTBM**. (a, f, k) Dark-field STEM images of the BHJ active layers "*as-cast*". (b, g, l) EELS maps of the BHJ active layers "*as-cast*"; SM donor-rich regions: red, SM acceptor-rich regions: green. (c, h, m) Dark-field STEM images of the "optimized" BHJ active layers. (d, i, n) EELS maps of the "optimized" BHJ active layers; SM donor-rich regions: red, SM acceptor-rich regions: green. (e, j, o) Low-dose HR-TEM images of the "optimized" BHJ active layers, emphasizing the observation of crystallites across the films. Scale bars: (a-n) 500 nm; (e, j, o) 20 nm.

in Figure 3 indicates that donor and acceptor counterparts are forming networks on various scales. The energy loss spectra pertaining to **DR3, SMPV1, BTR** and to **IDTTBM** (range: 2-8 eV) are shown in Figure S12-14, allowing to distinguish between SM donor and nonfullerene acceptor across the BHJ active layers. In the dark-field scanning TEM mode (STEM), our EELS analyses (Figures 3b, 3g and 3l; also see neat materials in Figures S12-S14), provide a clear map of the phase-separated networks occurring across *"as-cast"* All-SM BHJ active layers; Red: SM donor-rich domains, Green: SM acceptor-rich domains (scale bars: 500 nm). Here, SM donor-rich domains as large as ca. 200 nm can be observed in the blend films (also see Fig. S12a-14a (neat materials), Fig. S17-20, and Table S9). In contrast, "optimized" All-SM BHJ active layers (Figures 3d, 3i and 3n) show significantly finer-scale networks of SM donor- and SM acceptor-rich phases, indicating that the presence of DIO in the processing solution effectively impacts the lengthscale of the donor-acceptor network formed. However, as seen from **DR3**-based BHJs in Figure S15, larger-sized SM donor regions may grow when the extent of DIO is increased to >1%, resulting in donor-rich domains larger than *ca.* 400 nm when up to 10% DIO is used (Fig. S15). Interestingly, considering **BTR**-based BHJs, Figures S16 show that SM acceptor-rich domains have a tendency to prevail when the extent of DIO is increased, indicating that **DR3** and **BTR** have distinct network-forming propensities in the BHJ active layers with **IDTTBM**. Overall, Figures 3d, 3i and 3n emphasize the notable reduction in phase-separation lengthscale across all three BHJ active layers, as donor-acceptor intermixing improves in the presence of DIO (when quantities remain <1%, v/v), yielding BHJ solar cells with improved morphologies and, in turn, higher PCEs (Table 2). The HR-TEM images provided in Figures 3e, 3j and 3o

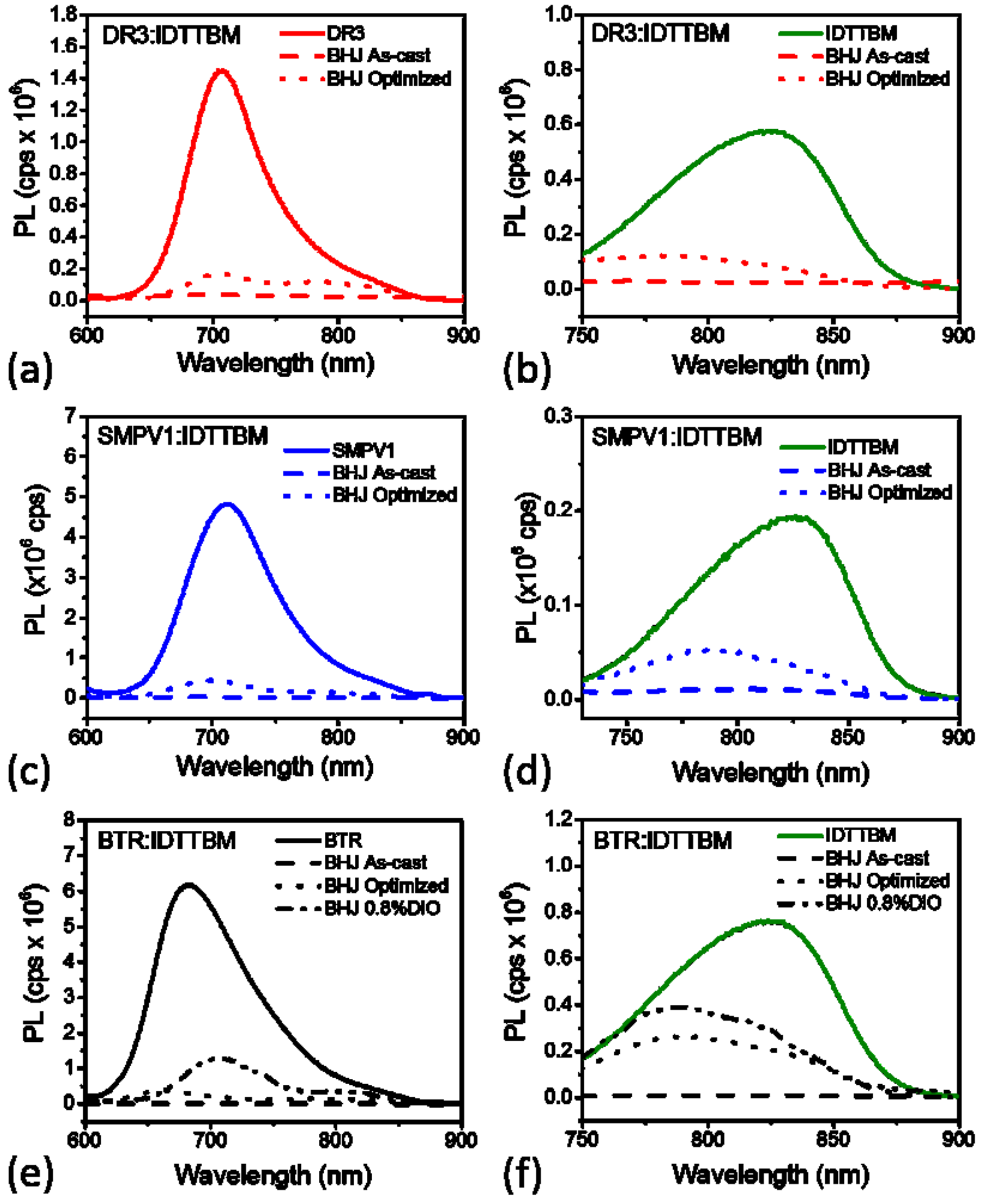

Figure 4. Photoluminescence (PL) quenching data for the SM donors **DR3, SMPV1** and **BTR** and the nonfullerene acceptor **IDTTBM** in neat films (reference; w/o additive) (solid lines), and in the presence of their donor/acceptor counterpart (dashed lines) in "*as-cast*" (w/o additive) and in "optimized" BHJ active layers (0.8% DIO, v/v). **(a) DR3**:**IDTTBM**, excitation at 580 nm, **(b) DR3**:**IDTTBM**, excitation at 700 nm, **(c) SMPV1**:**IDTTBM**, excitation at 580 nm, **(d) SMPV1**:**IDTTBM**, excitation at 700 nm, **(e) BTR**:**IDTTBM**, excitation at 570 nm, **(f) BTR**:**IDTTBM**, excitation at 700 nm.

indicate that crystallites of *ca.* 40-50 nm are forming in optimized BHJ active layers (cf. experimental details in the SI (Section 5)). Based on our combined X-ray diffraction (XRD) and thin-film grazing incidence X-ray scattering (GIXS) analyses respectively provided in Figures S21-22 and S26 the crystallites observed by HR-TEM stem from the self-organization of the SM donors **DR3, SMPV1,** and **BTR (**π-π distances: *ca.* 3.58 Å for **DR3** and **SMPV1** (in-plane), and *ca.* 3.72 Å for **BTR** (out-of-plane)**)**; whereas the SM acceptor **IDTTBM** does not show any evident sign of crystalline behavior based on these analyses. Since the absorption spectra (Fig. 1a) and PL patterns (Fig. 4) of the SM donors **DR3, SMPV1** and **BTR**, and that of the SM acceptor **IDTTBM**, lie in regions of sufficiently distinct wavelengths, the donor and acceptor components can be individually excited at different wavelengths (580 nm and 700 nm, respectively). As illustrated in Figure 4, considering the excitation of the SM donor-rich domains (Fig. 4a, 4c and 4e), the PL quenching efficiencies of the "optimized" BHJ active layers remain >90% in the presence of the nonfullerene acceptor **IDTTBM**. However, probing the SM acceptor-rich domains (Fig. 4b, 4d and 4f), it can be noted that the PL quenching efficiencies are more modest: 85% and 82% in blends with **DR3** and **SMPV1**, and <70% in blends with **BTR**. These observations suggest that exciton diffusion and charge transfer at the donor-acceptor interfaces occur relatively effectively within the SM donor-rich domains (more crystalline as shown in Fig. 3e, 3j and 3o), but that these processes are not as effective within SM acceptor-rich

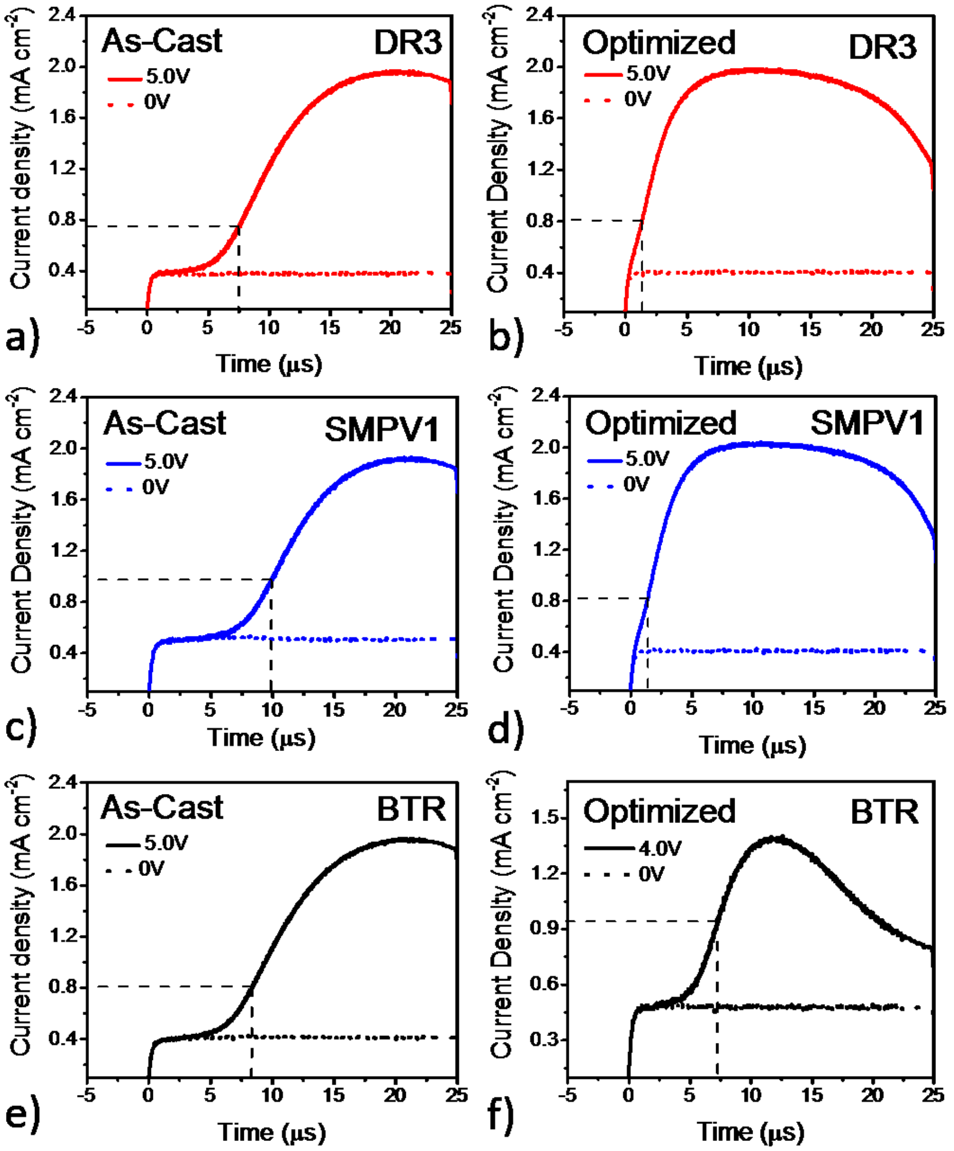

Figure 5. Experimental dark current MIS-CELIV transients for hole-only diodes (ITO/MgF_2/SM:**IDTTBM**/MoO_3/Ag) made from **(a)** **DR3:IDTTBM**-based “*as-cast*” blends, **(b)** **DR3:IDTTBM**-based “optimized” blends, **(c)** **SMPV1:IDTTBM**-based “*as-cast*” blends, **(d)** **SMPV1:IDTTBM**-based “optimized” blends, **(e)** **BTR:IDTTBM**-based “*as-cast*” blends, and **(f)**

BTR:IDTTBM-based "optimized" blends. Device processing conditions detailed in Table 2; data obtained for electron-only diodes provided in the SI, Figure S19.

regions. In turn, the PL quenching experiments indicate that further improving the All-SM active layer morphologies may substantially improve the photocurrents in actual BHJ solar cells.

Efficiency of carrier transport can be correlated to morphological effects in BHJ active layers.[6, 39] To probe carrier transport across the All-SM blends with **DR3, SMPV1** and **BTR**, we turned to "metal-insulator-semiconductor carrier extraction" measurements using linearly increasing voltage transients (MIS-CELIV; cf. experimental details in the SI (Section 5), including Fig. S23-S25 and Tables 3).[40-42] The results of those analyses are provided in Figure 5 and Table 3. Figure 5 shows the dark current density-voltage characteristics (at room temperature) for "*as-cast*" and "optimized" All-SM active layers in hole-only MIS diodes (ITO/MgF_2/SM:**IDTTM**/MoO_3/Ag) and electron-only MIS diodes (ITO/MgF_2/SM:**IDTTBM**/Ca/Al). The thick layers of MgF_2 (*ca.* 80 nm; cf. details in Fig. S23) deposited on ITO are intended to block a specific carrier type (holes or electrons) while only the oppositely-charged carrier is extracted and analyzed. Our analyses summarized in Table 3 indicate that hole (μ_h) and electron (μ_e) mobilities for "*as-cast*" active layers fall into the range 1-2 x 10^{-5} cm^2 V^{-1} s^{-1}. In "optimized" active layers cast with DIO (0.8%, v/v), μ_h values for **DR3**/**SMPV1**-based active layers reach *ca.* 4.5 x 10^{-4} cm^2 V^{-1} s^{-1}, which are approximately one order of magnitude higher than those of **BTR**-based active layers (*ca.* 1.7 x 10^{-5} cm^2 V^{-1} s^{-1}); μ_e values in range of 1-3.5 x 10^{-4} cm^2 V^{-1} s^{-1} scale comparably across all "optimized" BHJ active layers. The notable difference in hole mobilities between **DR3**/**SMPV1**- and **BTR**-based active layers parallel the solar cell efficiency differences outlined earlier in Table 2: PCEs of *ca.* 4.5%

Table 3. Carrier mobility estimates obtained by MIS-CELIV analyses for "*as-cast*" and "optimized" for "All-SM" active layers made from **DR3**, **SMPV1** and **BTR**, in blends with the nonfullerene SM acceptor **IDTTBM**.

SM Donor[a]	Active Layer	μ_h [cm^2 V^{-1} s^{-1}]	μ_e [cm^2 V^{-1} s^{-1}]	μ_h/μ_e
DR3	as-cast	1.4 x 10^{-5}	1.0 x 10^{-5}	1.4
	optimized	4.5 x 10^{-4}	1.4 x 10^{-4}	3.2
SMPV1	as-cast	1.0 x 10^{-5}	1.0 x 10^{-5}	1.0
	optimized	4.5 x 10^{-4}	1.5 x 10^{-4}	3.0
BTR	as-cast	1.4 x 10^{-5}	1.5 x 10^{-5}	0.93
	optimized	1.7 x 10^{-5}	3.3 x 10^{-4}	0.052

[a]The "*as-cast*" and "optimized" conditions are described in Table 2.

for **DR3/SMPV1**-based devices vs. PCEs of <2.5% **BTR**-based optimized BHJ solar cells. We also note that the imbalance between hole and electron mobilities in the **BTR**-based BHJ thin films (μ_h/μ_e = 0.052 vs. 3.21 for **DR3**/**SMPV1**-based films) is likely to be at the origin of significant charge build-up in optimized BHJ device, limiting the J_{SC}; interpretation in agreement with the figures of merit outlined for **BTR**-based device in Table 2: low J_{SC} values <6 mA/cm^2.

To investigate the carrier recombination kinetics in "*as-cast*" and optimized BHJ active layers with **DR3**, **SMPV1** and **BTR**, and the nonfullerene SM acceptor **IDTTBM**, we examined the variations of J_{SC} under various light intensities (cf. details in SI, Section 5). Prior studies have described how bimolecular recombination losses in BHJ solar cells can be estimated

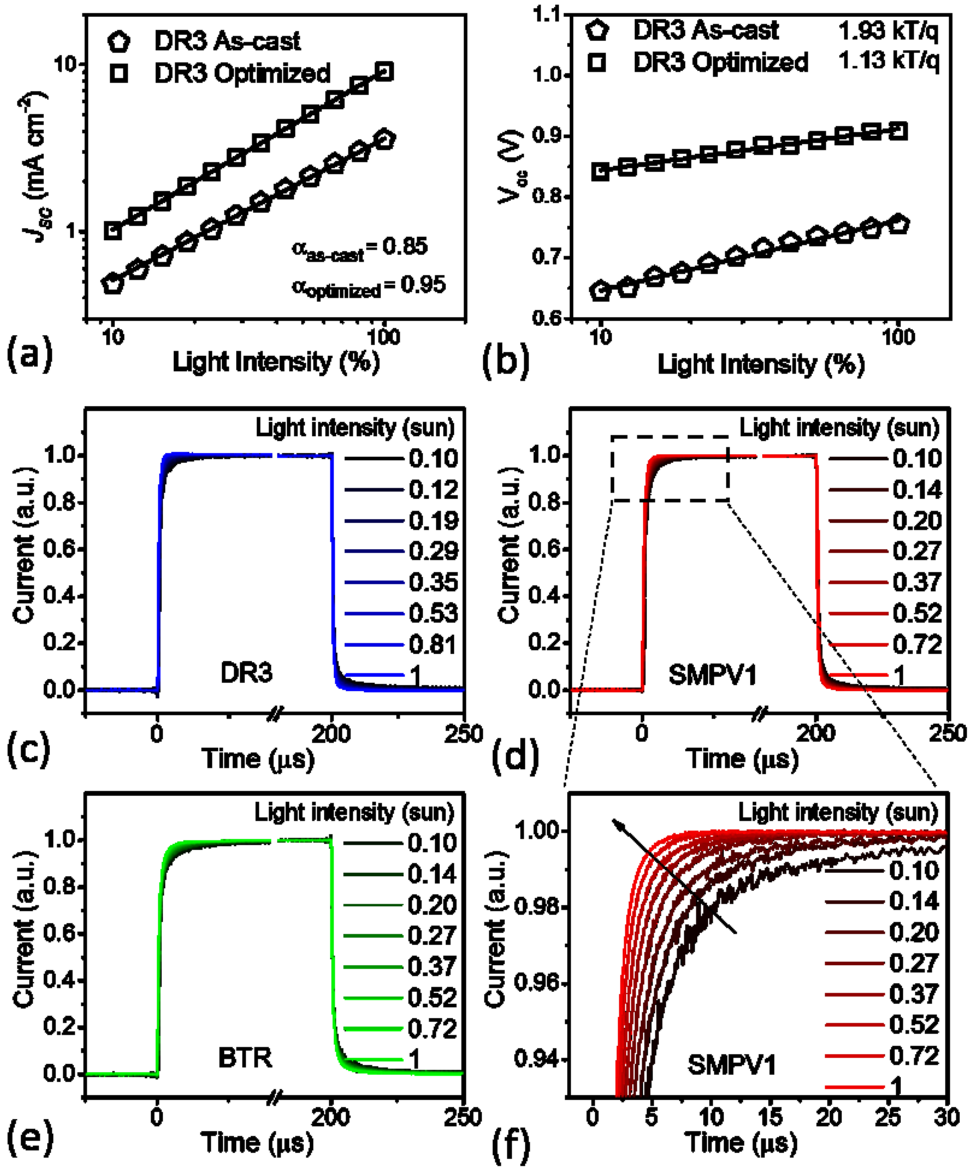

Figure 6. **(a)** J_{SC} *vs.* light intensity plots for **DR3**–based BHJ devices with various active layer thicknesses. **(b)** V_{OC} *vs.* light intensity plot for **DR3**–based BHJ devices with various active layer thicknesses. Transient short-circuit current (normalized) in response to a 200 µs white light (LED)

pulse for **(c) DR3 (d) SMPV1 (e) BTR** –based BHJ devices. **(f)** Turn-on dynamics for **SMPV1**-based device. The black arrows emphasize the dependence of the device short-circuit current characteristics as a function of light intensities (provided in terms of equivalent sun; cf. details in the SI). The solid lines in **(a)** and **(b)** correspond to fits to the data according to $J_{sc} \propto I^{\alpha}$ and $\delta Voc = \frac{nkT}{q} \ln I$, respectively. Analyses performed with a white LED with a maximum irradiance of 200 mW/cm^2. In accounting for spectral mismatch, 70% of the maximum irradiance of the white-light LED was used to reproduce the J_{SC} values normally achieved under standard AM1.5G solar illumination (100 mW/cm^2).

by fitting J_{SC} vs. light intensity data plotted in log scales, using the power law equation $J_{sc} \propto I^{\alpha}$, where α is the power factor. In short, a value of α equal to unity reflects weak/no bimolecular recombination (in this instance, most carriers are swept out prior to recombining),[38-39] whereas smaller α values indicate a competition between carrier recombination and extraction, whereby recombination yields impinges on the device photocurrent. Figures 6 and S27 illustrate the dependence of J_{SC} on light intensity for the All-SM BHJ devices cast without processing additive (no DIO), and in the presence of additive (cf. optimized conditions defined in Table 2). For "*as-cast*" **BTR**-based BHJ active layers in Figure S27b, the fits to the J_{SC} vs. light intensity data yield α values of 0.81, indicating appreciable recombination losses. In contrast, optimized **BTR**-based BHJs yield α values of 0.95, indicative of a more favorable regime whereby carrier extraction proceeds with notably suppressed recombination losses. Likewise, α values inferred from the fits to the J_{SC} vs. light intensity data in Figures 6a and S27a for "*as-cast*" **DR3**- and **SMPV1**-based BHJ active layers increase from 0.85 and 0.86, to 0.95 and 0.96, respectively, indicating that bimolecular recombination can be nearly suppressed upon systematic optimization of the BHJ active layer morphologies. These results are consistent with the figures of merit summarized in Table 2 when comparing "*as-cast*" and optimized BHJ solar cells made with **DR3**, **SMPV1** and **BTR**. From these analyses, we note however that the lower J_{SC} <6 mA/cm^2 measured for **BTR**-based BHJ devices does not stem from a higher yield of bimolecular recombination under AM1.5G.

Figure 6b and S27c-d shows the variation of V_{OC} vs. light intensity in a natural log scale, with data fitted to $V_{OC} \propto nkT/q \ln(I)$, where k, T, and q are the Boltzmann constant, temperature in Kelvin, and the elementary charge, respectively. The parameter n (usually in the range of 1 to 2) reflects the presence/absence of carrier traps across the active layers or at interfaces with the electrodes.[44-46] Any deviations from n = 1 (trap-free condition) point to the existence of recombination effects and, more specifically, to the existence of trap-assisted recombination. In Figure 6b, the V_{OC} vs. light intensity data for "*as-cast*" **DR3**-based devices shows a slope of n=1.93 kT/q, indicating a significant extent of trap-assisted recombination near V_{OC}. In optimized active layers, inferred n values are reduced to 1.13, showing that trap-assisted recombination is suppressed as more favorable morphologies are achieved. As shown in Figures S27c and S27d, *n* values for optimized **SMPV1**- and **BTR**-based BHJ active layers are similarly suppressed to 1.18 and 1.13, respectively.

Further insights into carrier transport and, in particular, on whether carrier traps affect the transport in BHJ active layers can be inferred from transient photocurrent (TPC) measurements. TPC experiments have previously been used to investigate the trapping and detrapping rates in polymer-fullerene,[47-48] "all-polymer",[47, 49] and hybrid BHJ solar cells.[50] Figures 6c-f examine the turn-on and turn-off dynamics of optimized BHJ active layers with **DR3**, **SMPV1** and **BTR** using long light pulse excitations (200 µs; cf. details in the SI, including Fig. S28), allowing the current density to reach the steady-state conditions comparable to those used for the light intensity dependence analysis previously discussed (Fig. 6a-b). For all three All-SM systems, the turn-on and turn-off dynamics are fast and varying the light intensity result in negligible changes in the current response. As shown in Figure 6f, a closer examination of the current response confirms that the light dependence behavior is modest. At 1 sun condition, the rise/fall time (defined as the time taken to go from 10% to 90% of the response) is respectively 1 µs, 1.5 µs, 2.1 µs for **DR3**, **SMPV1** and **BTR** –based optimized active layers. The modest light dependence behavior may stem from the charge density dependence of the carrier mobility. Importantly, the fast turn-on/turn-off behavior observed for all three All-SM systems, and near-"transient-peak-free" curves and rise/fall times, indicate that carrier trapping and/or detrapping effects are not limiting factors significantly influencing BHJ solar cell performance.

In BHJ active layers for which adequately mixed donor-acceptor morphologies are apparent via EELS mapping analyses in STEM mode (Fig. 3), the presence of poorly connected small-sized domains and aggregate trap states are difficult to discern, yet those can effectively lower the EQE/IQE in actual BHJ solar cells. The presence of these morphological features can be inferred from reverse bias analyses (described below) and carrier transport measurements (discussed in earlier section). In Figure 7, the photocurrent of optimized **DR3**- and **BTR**-based

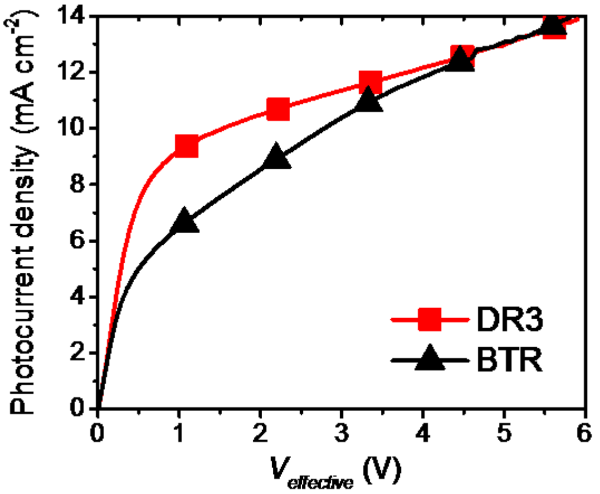

Figure 7. Photocurrent vs. effective applied voltage (V_0-V_{app}) for optimized BHJ devices made from **DR3** and **BTR**, respectively. Photocurrent densities are obtained from subtracting device current densities under illumination and in the dark, respectively, and $V_{effective}$ from subtracting the compensation voltage (voltage at J_{photo}= 0) and the applied bias, respectively. The optimized conditions are described in Table 2.

BHJ solar cells is plotted as a function of the effective applied voltage (V_{eff}). Here, the characteristic photocurrent of **BTR**-based BHJ devices shows a pronounced field-dependent behavior across the whole V_{eff} range (0-6V); for optimized **DR3**-based BHJ devices, the characteristic photocurrent does not follow the same slop across the same V_{eff} range and it rapidly reaches higher values at lower biases (comprising those relevant to solar cell operation; *e.g.* 9.2 mA cm^{-2} at 1 V vs. 6.4 mA cm^{-2} in **BTR**-based devices). These results suggest that charges can be relatively efficiently separated and extracted in **DR3**-based BHJs, while optimized **BTR** BHJs remain hindered by morphological effects. From our prior MIS-CELIV analyses (Fig. 5 and Table 3), we shall also recall that hole mobilities in optimized **BTR**-based BHJ active layers are significantly lower that those in **DR3**-based BHJs (1.7×10^{-5} cm^2 V^{-1} s^{-1} vs. 4.5×10^{-4} cm^2 V^{-1} s^{-1}, respectively), an observation that parallels the expectation of unfavorably connected donor-rich domains and aggregate trap states across **BTR**-based active layers. While more detailed spectroscopic and morphological analyses are beyond the scope of this concise report, future work should shed light on the morphology-correlated charge dynamics in those systems.

3. Conclusion

In summary, comparing the efficiency patterns of the well-defined SM donors **DR3**, **SMPV1**, and **BTR** – used in conjunction with the nonfullerene acceptor **IDTTBM** – in “All-SM” BHJ solar cells, we found that **DR3**- and **SMPV1**-based devices can achieve PCEs of up to *ca.* 4.5% (avg. 4.0%). While the side-chain manifold of their analogous **BTR** counterpart differs to a more significant extent, **BTR**-based BHJ solar cells are limited to lower figures of merit (PCEs <2.5%). Importantly, the outcome of our systematic EELS analyses in STEM mode indicates that "*as-cast*" BHJ morphologies are significantly coarser (SM domains as large as *ca.* 200 nm) than those of "optimized" BHJ solar cells, resulting in PCEs <1%. When the solution-processing additive 1,8-diiodooctane (DIO, 0.8% v/v) is used in the blend solutions, the phase-separation lengthscale of the donor-acceptor network improves dramatically and, in general, the carrier mobilities (estimated by MIS-CELIV) increase. While the carrier recombination analyses (light-dependence and TPC measurements) indicate that the nongeminate recombination effects in all-SM devices (**DR3**, **SMPV1** and **BTR**) are significantly reduced in "optimized" active layers compared to "*as-cast*" ones, the charge transport studies show that **DR3-** and **SMPV1**-based "All-SM" devices benefit from a greater balance in hole/electron mobilities (μ_h/μ_e = *ca.* 3 vs. 0.05) and higher carrier collection efficiencies compared to their **BTR** counterpart. This study also emphasizes the relevance of the nonfullerene SM acceptor **IDTTBM** for "All-SM" BHJ solar cells.

Supporting Information

Experimental methods, characterization, and additional figures and tables. Supporting Information is available from the Wiley Online Library or from the author.

Acknowledgements

The authors declare no competing financial interest. This publication is based upon work supported by the King Abdullah University of Science and Technology (KAUST) Office of Sponsored Research (OSR) under Award No. CRG_R2_13_BEAU_KAUST_1 and under the KAUST Solar Center programs. The authors also acknowledge concurrent support under Baseline Research Funding from KAUST. The authors thank KAUST ACL for technical support in the mass spectrometry analyses. Dr D.J. Jones acknowledges the Australian Renewable Energy Agency which funds the project grants within the Australian Centre for Advanced Photovoltaics. Responsibility for the views, information or advice expressed herein is not accepted by the Australian Government. R.-Z. Liang and M. Babics contributed equally to this work.

Received: ((will be filled in by the editorial staff))
Revised: ((will be filled in by the editorial staff))
Published online: ((will be filled in by the editorial staff))

References:

[1] P. Kovacik, G. Sforazzini, A. G. Cook, S. M. Willis, P. S. Grant, H. E. Assender, A. A. R. Watt, *Acs Appl Mater Inter* **2011**, *3*, 11.

[2] P. Kovacik, H. E. Assender, A. A. R. Watt, *Sol Energ Mat Sol C* **2013**, *117*, 22.

[3] B. Kan, Q. Zhang, M. M. Li, X. J. Wan, W. Ni, G. K. Long, Y. C. Wang, X. Yang, H. R. Feng, Y. S. Chen, *J Am Chem Soc* **2014**, *136*, 15529.

[4] B. Kan, M. M. Li, Q. Zhang, F. Liu, X. J. Wan, Y. C. Wang, W. Ni, G. K. Long, X. Yang, H. R. Feng, Y. Zuo, M. T. Zhang, F. Huang, Y. Cao, T. P. Russell, Y. S. Chen, *J Am Chem Soc* **2015**, 137, 3886.

[5] K. Sun, Z. Xiao, S. Lu, W. Zajaczkowski, W. Pisula, E. Hanssen, J. M. White, R. M. Williamson, J. Subbiah, J. Ouyang, A. B. Holmes, W. W. Wong, D. J. Jones, *Nat Commun* **2015**, *6*, 6013.

[6] K. Wang, R.-Z. Liang, J. Wolf, Q. Saleem, M. Babics, P. Wucher, M. Abdelsamie, A. Amassian, M. R. Hansen, P. M. Beaujuge, *Adv Funct Mater* **2016**, *26*, 7103.

[7] J. Wolf, M. Babics, K. Wang, Q. Saleem, R. Z. Liang, M. R. Hansen, P. M. Beaujuge, *Chem Mater* **2016**, *28*, 2058.

[8] J. Min, O. K. Kwon, C. Cui, J.-H. Park, Y. Wu, S. Y. Park, Y. Li, C. J. Brabec, *J. Mater. Chem. A* **2016**, *4*, 14234.

[9] Y. Lin, J. Wang, T. Li, Y. Wu, C. Wang, L. Han, Y. Yao, W. Ma, X. Zhan, *J. Mater. Chem. A* **2016**, *4*, 1486.

[10] H. Bai, Y. Wu, Y. Wang, Y. Wu, R. Li, P. Cheng, M. Zhang, J. Wang, W. Ma, X. Zhan, *J. Mater. Chem. A* **2015**, *3*, 20758.

[11] N. Liang, D. Meng, Z. Ma, B. Kan, X. Meng, Z. Zheng, W. Jiang, Y. Li, X. Wan, J. Hou, W. Ma, Y. Chen, Z. Wang, *Adv Energy Mater* **2017**, *7*, 1601664.

[12] L. Yang, S. Zhang, C. He, J. Zhang, H. Yao, Y. Yang, Y. Zhang, W. Zhao, J. Hou, *J Am Chem Soc* **2017**, *139*, 1958.

[13] C. M. Proctor, M. Kuik, T.-Q. Nguyen, *Progress in Polymer Science* **2013**, *38*, 1941.

[14] Y. Sun, G. C. Welch, W. L. Leong, C. J. Takacs, G. C. Bazan, A. J. Heeger, *Nat Mater* **2012**, *11*, 44.

[15] Y.-W. Su, S.-C. Lan, K.-H. Wei, *Materials Today* **2012**, *15*, 554.

[16] D. Deng, Y. J. Zhang, L. Yuan, C. He, K. Lu, Z. X. Wei, *Adv Energy Mater* **2014**, *4*, 1400538.

[17] T. S. van der Poll, J. A. Love; T. Q. Nguyen, G. C. Bazan, *Adv Mater* **2012**, 24, 3646.

[18] B. Kan, Q. Zhang, F. Liu, X. J. Wan, Y. C. Wang, W. Ni, X. Yang, M. T. Zhang, H. T. Zhang, T. P. Russell, Y. S. Chen, *Chem Mater* **2015**, *27*, 8414.

[19] M. M. Li, F. Liu, X. J. Wan, W. Ni, B. Kan, H. R. Feng, Q. Zhang, X. Yang, Y. C. Wang, Y. M. Zhang, Y. Shen, T. P. Russell, Y. S. Chen, *Adv Mater* **2015**, *27*, 6296.

[20] K. Wang, M. Azouz, M. Babics, F. Cruciani, T. Marszalek, Q. Saleem, W. Pisula, P. M. Beaujuge, *Chem Mater* **2016**, *28*, 5415.

[21] A. J. Heeger, *Adv Mater* **2014**, *26*, 10.

[22] S. D. Collins, N. A. Ran, M. C. Heiber, T.-Q. Nguyen, *Adv Energy Mater* **2017**, 1602242.

[23] A. Sharenko, C. M. Proctor, T. S. van der Poll, Z. B. Henson, T. Q. Nguyen, G. C. Bazan, *Adv Mater* **2013**, *25*, 4403.

[24] G. T. Feng, Y. H. Xu, J. Q. Zhang, Z. W. Wang, Y. Zhou, Y. F. Li, Z. X. Wei, C. Li, W. W. Li, *J Mater Chem A* **2016**, *4*, 6056.

[25] H. Bin, Y. Yang, Z. G. Zhang, L. Ye, M. Ghasemi, S. Chen, Y. Zhang, C. Zhang, C. Sun, L. Xue, C. Yang, H. Ade, Y. Li, *J Am Chem Soc* **2017**, *139*, 5085.

[26] M. Privado, V. Cuesta, P. D. L. Cruz, M. L. Keshtov, G. D. Sharma, F. Langa, *J Mater Chem A,* **2017**, *5*, 14259.

[27] W. Ni, M. Li, B. Kan, F. Liu, X. Wan, Q. Zhang, H. Zhang, T. P. Russel, Y. Chen, *Chem Commum* **2016**, *52*, 465.

[28] Y. F. eng, J. Liu, J. T. Wang, L. H. Liu, W. L. Li, H. K. Tian, X. J. Zhang, Z. Y. Xie, Y. H. Geng, F. S. Wang, *Adv Mater* **2014**, *26*, 471.

[29] P. M. Beaujuge, H. N. Tsao, M. R. Hansen, C. M. Amb, C. Risko, J. Subbiah, K. R. Choudhury, A. Mavrinskiy, W. Pisula, J. L. Bredas, F. So, K. Mullen, J. R. Reynods, *J Am Chem Soc* **2012**, *134*, 8944.

[30] C. Cabanetos, A. El Labban, J. A. Bartelt, J. D. Douglas, W. R. Mateker, J. M. J. Frechet, M. D. McGehee, P. M. Beaujuge, *J Am Chem Soc* **2013**, *135*, 4656.

[31] J. Warnan, C. Cabanetos, A. El Labban, M. R. Hansen, C. Tassone, M. F. Toney, P. M. Beaujuge, *Adv Mater* **2014**, *26*, 4357.

[32] H. Bin, Z. G. Zhang, L. Gao, S. Chen, L. Zhong, L. Xue, C. Yang, Y. Li, *J Am Chem Soc* **2016**, *138*, 4657.

[33] D. Baran, R. S. Ashraf, D. A. Hanifi, M. Abdelsamie, N. Gasparini, J. A. Rohr, S. Holliday, A. Wadsworth, S. Lockett, M. Neophytou, C. J. Emmott, J. Nelson, C. J. Brabec, A. Amassian, A. Salleo, T. Kirchartz, J. R. Durrant, I. McCulloch, *Nat Mater* **2017**, *16*, 363.

[34] J. Y. Zhou, Y. Zuo, X. J. Wan, G. K. Long, Q. Zhang, W. Ni, Y. S. Liu, Z. Li, G. R. He, C. X. Li, B. Kan, M. M. Li, Y. S. Chen, *J Am Chem Soc* **2013**, *135*, 8484.

[35] Y. S. Liu, C. C. Chen, Z. R. Hong, J. Gao, Y. Yang, H. P. Zhou, L. T. Dou, G. Li, Y. Yang, *Sci Rep* **2013**, *3*, 3356.

[36] S. Engmann, H. W. Ro, A. Herzing, C. R. Snyder, L. J. Richter, P. B. Geraghty, D. J. Jones, *J Mater Chem A* **2016**, *4*, 15511.

[37] Y. Chen, X. Zhang, C. Zhan, J. Yao, *Phy Status Solidi A* **2015**, *212*, 1961.

[38] A. Namepetra, E. Kitching, A. F. Eftaiha, I. G. Hill, G. C. Welch, *Phy Chem Chem Phy,* **2016**, *18*, 12476.

[39] G. C. Welch, L. A. Perez, C. V. Hoven, Y. Zhang, X. D. Dang, A. Sharenko, M. F. Toney, E. J. Kramer, T. Q. Nguyen, G. C. Bazan, *J Mater Chem* **2011**, *21*, 12700.

[40] A. Armin, M. Velusamy, P. L. Burn, P. Meredith, A. Pivrikas, *Appl Phys Lett* **2012**, *101*, 083306.

[41] G. Juska, N. Nekrasas, K. Genevicius, *J Non-Cryst Solids* **2012**, 358, 748.

[42] A. Armin,; G. Juska, M. Ullah, M. Velusamy, P. L. Burn, P. Meredith, A. Pivrikas, *Adv Energy Mater* **2014**, *4*, 1300954.

[43] L. J. A. Koster, M. Kemerink, M. M. Wienk, K. Maturova, R. A. J. Janssen, *Adv Mater* **2011,** *23*, 1670.

[44] S. R. Cowan, A. Roy, A. J. Heeger, *Physical Review B* **2010,** *82*, 245207.

[45] L. J. A. Koster, V. D. Mihailetchi, R. Ramaker, P. W. M. Blom, *Appl Phys Lett* **2005,** *86*, 123509.

[46] D. Zhao, M. Sexton, H.-Y. Park, G. Baure, J. C. Nino, F. So, *Adv Energy Mater* **2015,** *5*, 1401855.

[47] Z. Li, F. Gao, N. C. Greenham, C. R. McNeill, *Adv Funct Mater* **2011**, *21*, 1419.

[48] Z. Li, C. R. McNeill, *Journal of Applied Physics* **2011**, *109*, 074513.

[49] C. R. McNeill, I. Hwang, N. C. Greenham, *Journal of Applied Physics* **2009**, *106*, 024507.

[50] F. Gao, Z. Li, J. P. Wang, A. Rao, I. A. Howard, A. Abrusci, S. Massip, C. R. McNeill, N. C. Greenham, *Acs Nano* **2014**, 8, 3213.

Additive-Morphology Interplay & Loss Channels in "All-Small-Molecule" BHJ Solar Cells with the Nonfullerene Acceptor IDTTBM

Ru-Ze Liang, Maxime Babics, Akmaral Seitkhan, Kai Wang, Paul Bythal Geraghty, Sergei Lopatin, Federico Cruciani, Yuliar Firdaus, Marco Caporuscio, David J. Jones, and

*Pierre M. Beaujuge**

Keywords: small molecules, nonfullerenes, bulk heterojunctions, solar cells, organic photovoltaics.

Table of contents entry:

A set of structurally analogous small molecule (SM) donors with distinct side-chain manifolds shows significant differences in their performance patterns in bulk-heterojunction (BHJ) devices with the nonfullerene SM acceptor IDTTBM. Reducing the lengthscale of the phase-separated network between donor and acceptor effectively suppressses non-geminate recombination in the BHJ active layers and improves the carrier mobility balance.